



Topologically protected oxygen redox in a layered manganese oxide cathode for sustainable batteries

Ang Gao^{1,2,13}, Qinghua Zhang^{1,3,13}, Xinyan Li^{1,4}, Tongtong Shang^{1,2}, Zhixin Tang^{1,2}, Xia Lu⁵, Yanhong Luo¹, Jiarun Ding⁶, Wang Hay Kan^{7,8}, Huaican Chen^{7,8}, Wen Yin^{7,8}, Xuefeng Wang¹, Dongdong Xiao¹, Dong Su¹, Hong Li¹, Xiaohui Rong¹✉, Xiqian Yu¹, Qian Yu⁹, Fanqi Meng¹⁰, Cewen Nan¹⁰, Claude Delmas¹¹, Liqun Chen¹, Yong-Sheng Hu^{1,3,4}✉ and Lin Gu^{1,2,12}✉

Manganese could be the element of choice for cathode materials used in large-scale energy storage systems owing to its abundance and low toxicity levels. However, both lithium- and sodium-ion batteries adopting this electrode chemistry suffer from rapid performance fading, suggesting a major technical barrier that must be overcome. Here we report a P3-type layered manganese oxide cathode $\text{Na}_{0.6}\text{Li}_{0.2}\text{Mn}_{0.8}\text{O}_2$ (NLMO) that delivers a high capacity of 240 mAh g^{-1} with outstanding cycling stability in a lithium half-cell. Combined experimental and theoretical characterizations reveal a characteristic topological feature that enables the good electrochemical performance. Specifically, the $-\alpha-\gamma-$ layer stack provides topological protection for lattice oxygen redox, whereas reversibility is absent in P2-structured NLMO, which takes an $-\alpha-\beta-$ configuration. The identified new order parameter opens an avenue towards the rational design of reversible Mn-rich cathode materials for sustainable batteries.

The sustainable route to green transportation and grid applications calls for integration between renewable energy and high energy-density lithium- (Li) and sodium- (Na) ion batteries with combined safety and cost advantages^{1,2}. Compared to cobalt (Co) and nickel (Ni), two major elements in commercial cathode materials, redox-active manganese could be an alternative and more favourable choice for large-scale energy storage systems owing to its abundance and environmental compatibility³. In particular, Li/Na-rich Mn-based cathodes exhibit excellent capacity and high potential ($>4 \text{ V}$ versus Li^+/Li or Na^+/Na), resulting from the extra lattice oxygen redox (LOR)^{4–7}. However, the poor cycling stability of LOR-related processes, including voltage hysteresis and voltage fade, hampers its practical use, as a result of the irreversible local structural transformation or lattice oxygen loss^{8–10}. The stability and/or reversibility of LOR is correlated closely with the atomic structure or the local oxygen coordination environment, as elaborated by various theories, including the oxygen lone-pair states^{11–13}, reductive coupling mechanism^{14–17}, O–O dimer^{18,19}, ligand-to-metal charge transfer¹³ and critical oxygen hole²⁰ theories, as well as a number of other theories^{21–26}. Thus, exploring crystal structures compatible with reversible LOR in Mn-rich oxides is desirable to meet the demand for sustainable energy storage.

At present, the correlation between specific atomic structures with reversible LOR in electrode materials has not been well established. Kang and coworkers²⁷ found that transition metal (TM) layer stacks can control the voltage decay of LOR processes by comparing

O2- and O3-type $\text{Li}_x(\text{Li}_{0.2}\text{Ni}_{0.2}\text{Mn}_{0.6})\text{O}_2$. Li-excess disordered (rock salt) TM oxides, such as $\text{Li}_{1.211}\text{Mo}_{0.467}\text{Cr}_{0.3}\text{O}_2$ (ref. 28), $\text{Li}_{1.2}\text{Mn}_{0.4}\text{Ti}_{0.4}\text{O}_2$ (ref. 22) and $\text{Li}_{1.2}\text{Ni}_{0.333}\text{Ti}_{0.333}\text{Mo}_{0.133}\text{O}_2$ (ref. 29), have been reported with high capacities of around 300 mAh g^{-1} , also suggesting the positive effect of mixed alkali ions and TM ions on the LOR process³⁰. Compared to Li-ion batteries, Na layered-oxide cathodes are a more suitable system to probe the LOR mechanism, as they can maintain the well-ordered layer structure due to size mismatch between the TM and Na sites^{2,11,17,19,31}. Recent studies have demonstrated that the reversibility of LOR is related to the ordered structure or superstructure of the layered-oxide cathodes. In terms of the Na_2RuO_3 system, Yamada and coworkers³² proposed that the honeycomb ordering within TM layers can encourage reversible LOR. Further, they also demonstrated that a self-repairing layer stack on desodiation guarantees better reversibility of the electrode reaction³³. In $\text{Na}_{2/3}\text{Mg}_{1/3}\text{Mn}_{2/3}\text{O}_2$, the P2 stack can trigger a reversible collective distortion to stabilize the oxygen network, while the O2 stack suffers from voltage hysteresis accompanying the disproportionation of oxygen pairs¹⁷. Recently, Bruce and coworkers^{34,35} demonstrated that voltage hysteresis can be suppressed in LOR cathodes through a ribbon-ordered structure in TM layers that hinders in-plane migration of the TM. The above studies have focused largely on the structural design, involving intralayer atom configurations and interlayer stacks of electrode materials, and a further, more comprehensive theory could be required to control the critical electrochemical process.

¹Beijing National Laboratory for Condensed Matter Physics, Institute of Physics, Chinese Academy of Sciences, Beijing, China. ²School of Physical Sciences, University of Chinese Academy of Sciences, Beijing, China. ³Yangtze River Delta Physics Research Center Co. Ltd, Liyang, China. ⁴College of Materials Science and Opto-Electronic Technology, University of Chinese Academy of Sciences, Beijing, China. ⁵School of Materials, Sun Yat-sen University, Guangzhou, China. ⁶School of Physics and Engineering, Zhengzhou University, Zhengzhou, China. ⁷Spallation Neutron Source Science Center, Dongguan, PR China. ⁸Institute of High Energy Physics, Chinese Academy of Sciences, Beijing, PR China. ⁹School of Materials Science and Engineering, Zhejiang University, Hangzhou, China. ¹⁰State Key of Laboratory of New Ceramics and Fine Processing, School of Materials Science and Engineering, Tsinghua University, Beijing, China. ¹¹Université de Bordeaux, Bordeaux INP, ICMCB UMR 5026, CNRS, Pessac, France. ¹²Songshan Lake Materials Laboratory, Dongguan, China. ¹³These authors contributed equally: Ang Gao, Qinghua Zhang. ✉e-mail: rong@iphy.ac.cn; yshu@iphy.ac.cn; lgu@iphy.ac.cn

Over the past decade, topological structures have become an important research area in materials science and condensed matter physics^{36,37}. More intriguing topological structures have been discovered, thus opening up a new world of materials science and fundamental physics³⁸, including for energy storage materials³⁹. For instance, the topological feature of honeycomb-layered oxides has been reported to enable good electrochemical performance in rechargeable batteries⁴⁰. Ceder and coworkers demonstrated that a non-topotactic reaction can improve the rate capability in a Li-rich, cation-disordered, rock-salt cathode⁴¹. There is a growing awareness of the role of topological structures in improving battery performance and even LOR-related processes. Further investigations into these topological structures are urgently needed to explore structural stability and reversible LOR in layered cathodes.

Here, the key role of topological protection in enhancing the reversibility of LOR is established by comparing two closely related intercalation cathodes, P2- and P3- $\text{Na}_{0.6}\text{Li}_{0.2}\text{Mn}_{0.8}\text{O}_2$ (NLMO). The P3-NLMO cathode presents good reversibility of LOR in the Na half-cell, and delivers a high capacity of $\sim 240 \text{ mAh g}^{-1}$ with outstanding capacity retention performance in the Li half-cell. The experiment and theoretical calculations demonstrate that the topological feature of the $-\alpha-\gamma-$ stack provides topological protection for the reversibility of LOR on cycling in P3-NLMO, but that the $-\alpha-\beta-$ stack in P2-NLMO does not. The topological order $R^T = [1\ 3\ 5\ \dots\ 2q + 1]$ is utilized to elucidate the origin of the protected topological states in the P3-NLMO structure, which differs from the conventional phase definition (O- or P-type). Overall, the findings highlight the distinct role of topological protection in the reversible anionic redox of Mn-rich cathode materials for sustainable Li/Na-ion batteries.

Results

Structure and electrochemistry of P2- and P3-NLMO. The ribbon ordering in the TM layer, which presents a $(\dots\text{Li-4Mn-Li}\dots)$ sequence viewed along the [100] direction⁷, as shown in Fig. 1a, can inhibit first-cycle voltage hysteresis by suppressing manganese disorder and O_2 formation in the $\text{Na}_{0.6}[\text{Li}_{0.2}\text{Mn}_{0.8}]\text{O}_2$ cathode³⁴. Here, ribbon-ordered P2- and P3- $\text{Na}_{0.6}[\text{Li}_{0.2}\text{Mn}_{0.8}]\text{O}_2$ materials were synthesized using a facile high-temperature solid-state reaction¹⁹ and subsequently labelled as P2-NLMO and P3-NLMO. In P2- and P3-type structures, the oxygen columns exhibit ABBA-stack and ABCCA-stack sequences, respectively, along the [001] direction (Fig. 1b). The Rietveld-refined neutron diffraction profiles of the P2- and P3-NLMO samples present complete alignment with the calculated P2- and P3-type layered structures (Supplementary Data 1), as shown in Fig. 1c,d, showing good refinements (low weighted R profile (wRp) values). The lattice parameters of P2-NLMO were refined as $a = 9.886 \text{ \AA}$, $b = 7.548 \text{ \AA}$, $c = 11.497 \text{ \AA}$, $\alpha = 76.25^\circ$, $\beta = 90.28^\circ$ and $\gamma = 109.11^\circ$; those of P3-NLMO were refined as $a = 9.853 \text{ \AA}$, $b = 7.549 \text{ \AA}$, $c = 16.916 \text{ \AA}$, $\alpha = 83.60^\circ$, $\beta = 82.15^\circ$ and $\gamma = 70.85^\circ$. The refinement results are shown in Supplementary Tables 1 and 2. Meanwhile, the Rietveld-refined X-ray diffraction profiles were also employed to verify the structures of P2- and P3-NLMO samples (Supplementary Fig. 1a,b). On the basis of the unit cell, the diffraction peaks belonging to the superstructure were indexed as (010), (012), ($\bar{2}11$), ($2\bar{1}1$), (0 $\bar{1}2$), (022) and ($2\bar{1}\bar{1}$) planes for P2-NLMO, and (0 $\bar{1}1$), (211), ($20\bar{1}$), ($2\bar{1}2$), (223) and ($2\bar{1}3$) planes for P3-NLMO (Supplementary Figs. 1–3).

Figure 1e,f shows the first ten charge–discharge curves of P2- and P3-NLMO cycled in the voltage range 3.5–4.5 V at 10 mA g^{-1} . Capacities of 106 and 73 mAh g^{-1} were obtained in the first charge–discharge process of P2-NLMO, corresponding to 0.36 and 0.25 mol Na^+ ions (Fig. 1e). After ten cycles, only 0.30 mol Na^+ ions were retained in P2-NLMO, indicating rapid performance degradation. Meanwhile, P3-NLMO returned capacities of 105 and 73 mAh g^{-1} in the first charge–discharge process, corresponding to 0.36 and

0.25 mol Na^+ ions (Fig. 1f). After ten cycles, however, 0.40 mol Na^+ ions were retained in P3-NLMO, indicating comparatively excellent performance. To further quantify the contents of Li^+ and Na^+ ions, inductively coupled plasma-mass spectroscopy (ICP-MS) analysis was employed. The results (Supplementary Table 3) show that 0.48 and 0.32 mol of Na remained after one and ten cycles, respectively, in P2-NLMO. In addition, 0.49 and 0.40 mol of Na remained after one and ten cycles, respectively, in P3-NLMO. The ICP results are consistent with those from electrochemistry. Meanwhile, the Li contents (0.2 mol of Li) were shown to be essentially unchanged within ten cycles, according to the ICP results. With increase in the number of cycles, the reversible Na^+ ions decreased from 0.25 to 0.16 mol in P3-NLMO, and from 0.25 to 0.08 mol in P2-NLMO (Supplementary Fig. 4) according to the electrochemical results. Thus, it can be concluded that the capacity of P3-NLMO after ten cycles was almost twice that of P2-NLMO. It is worth noting that the reversible capacity (3.5–4.5 V) of both materials was mainly provided by LOR^{19,34,42} (for details see ‘Oxygen redox analysis’ in Methods). Hence, the inferior capacity retention of P2-NLMO indicated the irreversibility of the LOR process during cycling. Moreover, compared with P3-NLMO, the voltage polarization of P2-NLMO gradually increased with cycling, implying the irreversibility of the LOR process.

Topological characteristics of P2- and P3-NLMO. P2-NLMO exhibits inferior cycling stability compared with P3-NLMO, although both have a ribbon-ordered structure in the TM layer. Here, the stacking characteristics of both structures were analysed to explain the origin of this discrepancy, which can affect battery performance significantly^{10,27,43,44}. In addition to the intrinsic stacking differences between P2 and P3 structures (Fig. 1b), there are three possible stacking models based on the incorporation of Li^+ ions in the TM layer, namely, $-\alpha-\alpha-$, $-\alpha-\beta-$ and $-\alpha-\gamma-$ sequences (Fig. 2a), with the three stacking models superimposed to form one-dimensional topological (ODT) structures, as shown in Fig. 2b. In terms of the P2 structure, an $-\alpha-\alpha-$ model can exist in a P2-type unit cell ($1 \times 1 \times 1$) with two TMO_6 layers, whereas $-\alpha-\beta-$ and $-\alpha-\gamma-$ models generate the topological structure ($1 \times 1 \times 5$) along the out-of-plane with ten TMO_6 layers, as shown in the left panel of Fig. 2b. Similarly, in the P3 structure, an $-\alpha-\alpha-$ model can exist in a P3-type unit cell ($1 \times 1 \times 1$) with three TMO_6 layers, whereas $-\alpha-\beta-$ and $-\alpha-\gamma-$ models generate the topological structure ($1 \times 1 \times 5$) along the out-of-plane with 15 TMO_6 layers, as shown in the right panel of Fig. 2b. The ODT structures of pristine P2- and P3-NLMO were predicted to be $-\alpha-\beta-$ and $-\alpha-\gamma-$ stacks, respectively, by density functional theory (DFT) calculations (for details see ‘ODT structures’ in Methods) as shown in Supplementary Figs. 5–11. Figure 2c,f shows the ODT structures and Na sites of the optimized P2- and P3-NLMO from the side and top views.

The contrast in the high-angle annular dark-field-scanning transmission electron microscope (HAADF-STEM) images varied according to the atomic number in terms of a $Z^{1.7}$ dependency⁴⁵, which is more sensitive to heavy atoms (for example, Mn). The HAADF-STEM image of pristine P2-NLMO (Fig. 2d and Supplementary Fig. 12) revealed the ribbon-ordered structure of a TM layer with four-atom dumb-bells (Mn–Mn–Mn–Mn). More importantly, the $-\alpha-\beta-$ stacks (Fig. 2a) were revealed clearly in Fig. 2d (the brown area), which was consistent with the results of DFT calculations. Furthermore, various Na sites were detected by annular bright-field (ABF)-STEM analysis, which is more sensitive to lighter atoms⁴⁶ (Fig. 2e). The Na-ion distribution (black spots in the Na layer) was in good agreement with the theoretical predictions, as shown in Fig. 2c and the insert of Fig. 2e. The HAADF-STEM image of pristine P3-NLMO (Fig. 2g and Supplementary Fig. 13) also revealed the ribbon-ordered structure of a TM layer with largely $-\alpha-\gamma-$ and $-\alpha(-\gamma)-$ stacks (cyan area in

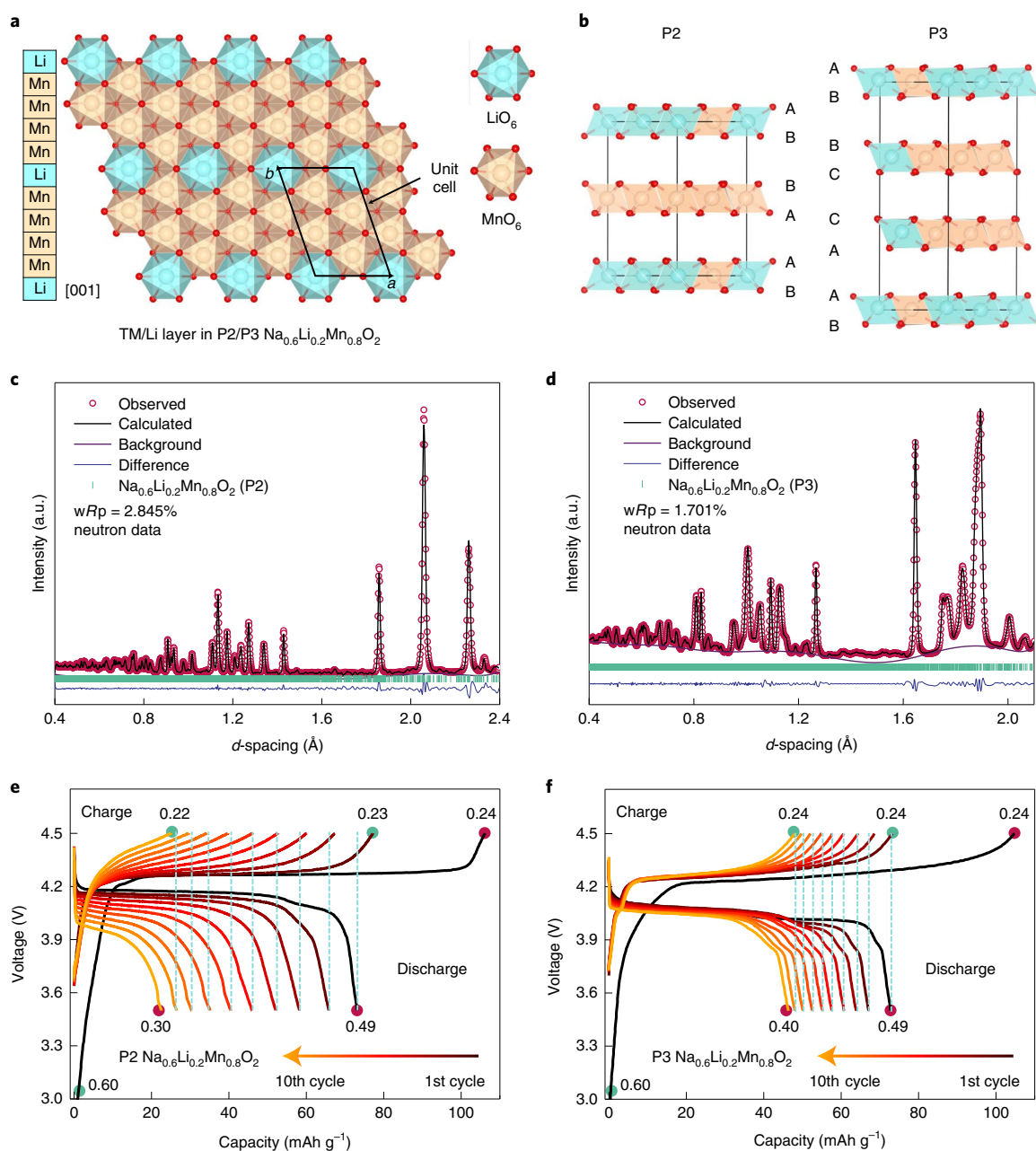


Fig. 1 | Ribbon-ordered structure and electrochemistry of P2- and P3-Na_{0.6}Li_{0.2}Mn_{0.8}O₂ cathode materials. **a**, Ribbon-ordered structure (---Li-4Mn-Li---) of the TM layer. **b**, Illustrations of P2- and P3-type structures. **c,d**, Refinement results of the neutron diffraction data of P2- (**c**) and P3-NLMO (**d**) samples using the structural model from DFT calculations, in which the red dots represent the experimental pattern; black line the calculated pattern; purple line the background curve; blue line the difference curve; and green bars the Bragg reflections. **e,f**, Capacity-voltage curves of ten cycles for P2- (**e**) and P3-NLMO (**f**) in a Na half-cell, with the Na content (*x*) near the green or red circle at various states of charge or discharge in Na_{*x*}Li_{0.2}Mn_{0.8}O₂.

Fig. 2g) and a small number of $-\alpha\beta-$ stacks, which was also consistent with the results of DFT calculations. The slight stacking fault was confirmed in our previous work¹⁹. The Na-ion distribution (black spots in the Na layer) was also in good agreement with the theoretically predicted models, as shown in Fig. 2f and the insert of Fig. 2h. Moreover, the Na-ion locations in both materials were also verified by refinement of the neutron diffraction, as displayed in Supplementary Tables 1 and 2.

Evolution of ODT structures on cycling. Then, we traced the evolution of ODT structures on cycling using STEM analysis (Fig. 3 and Supplementary Fig. 14). Figure 3a–c presents the HAADF images of

the P2-NLMO samples in the first-charged (4.5 V versus Na⁺/Na), first-discharged (3.5 V versus Na⁺/Na) and tenth-discharged states, respectively. In the HAADF-STEM image of pristine P2-NLMO (Fig. 2d), the $-\alpha\beta-$ stacks of the TM layers were clearly visible (the brown area), which was also verified by DFT calculations. In contrast, the HAADF image of the charged samples (4.5 V versus Na⁺/Na) (Fig. 3a) revealed clear $-\alpha\gamma-$ stacks of the TM layers (the cyan area). In the STEM image of the first-discharged P2-NLMO (3.5 V versus Na⁺/Na) (Fig. 3b), the stacks of the TM layers partially returned to the pristine state ($-\alpha\beta-$) and partially preserved the stacking form of the charged state ($-\alpha\gamma-$). Surprisingly, the stacks of the TM layer were converted completely to $-\alpha\gamma-$ sequences after ten

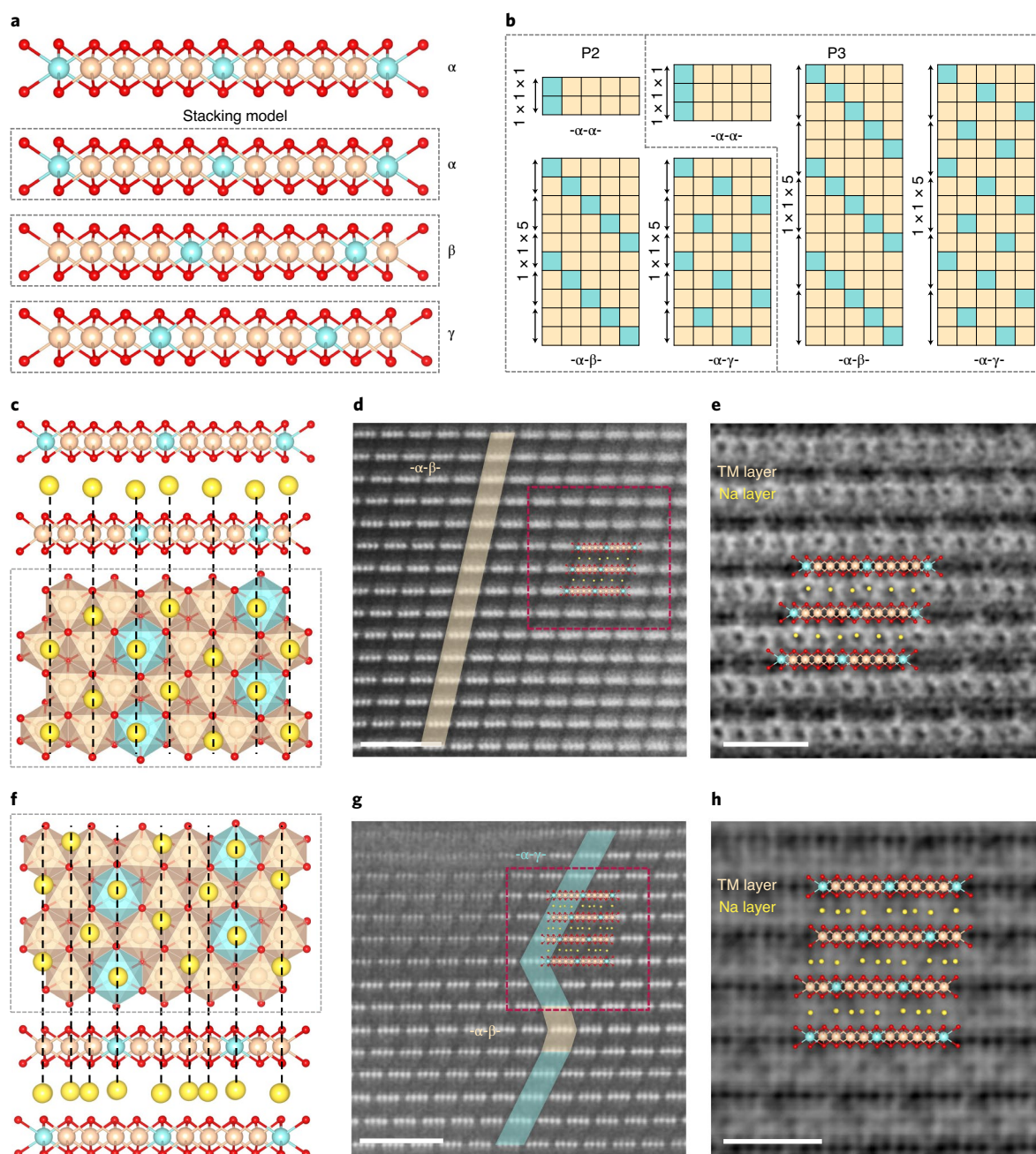


Fig. 2 | ODT structures and Na configurations in pristine P2- and P3-NLMO. **a**, Three stacking models of the TM layer including $-\alpha-\alpha-$, $-\alpha-\beta-$ and $-\alpha-\gamma-$ sequences. **b**, ODT structures of P2- and P3-NLMO induced by the stacking models, with the cyan and beige boxes representing the Li and Mn ions in the TM layer, respectively. **c–e**, P2-type. Optimized structure (side and top views) (**c**), HAADF-STEM (**d**) and ABF-STEM (**e**) images (the inset shows the optimized P2 structure). **f–h**, P3-type. Optimized structure (side and top views) (**f**), HAADF-STEM (**g**) and ABF-STEM (**h**) images (the inset shows the optimized P3 structure). The cyan ball is the Li ion, the brown ball the Mn ion, the yellow ball the Na ion and the red ball the O ion. Scale bars, 2 nm in **d,g** and 1 nm in **e,h**.

cycles (Fig. 3c). The STEM analysis unequivocally confirmed the irreversible interlayer stacking transformation from $-\alpha-\beta-$ to $-\alpha-\gamma-$ sequences during the successive charge and discharge of P2-NLMO. Figure 3d–f presents the HAADF images of the P3-NLMO samples in the first-charged (4.5 V versus Na^+/Na), first-discharged (3.5 V versus Na^+/Na) and tenth-discharged states, respectively. In contrast to P2-NLMO, the stacks of TM layers in P3-NLMO maintained $-\alpha-\gamma-$ sequences consistently during successive charge and discharge (Fig. 3d,e), even after ten cycles (Fig. 3f). The evolution of ODT structures was further detected by ex situ X-ray diffraction

(Supplementary Figs. 15–20 and Supplementary Note 1), which was consistent with the STEM analysis.

Topological protection mechanism. The ODT structures between the interlayers exhibited notable differences in P2- and P3-NLMO, in terms of both the pristine and the cycled samples. Similar to the constant topological features in multiferroic vortex domains^{47–49}, we introduced the topological protection of LOR to elucidate the electrochemical performance of P2- and P3-NLMO by first-principles calculations. Figure 4a–d shows the evolution of the ODT structures

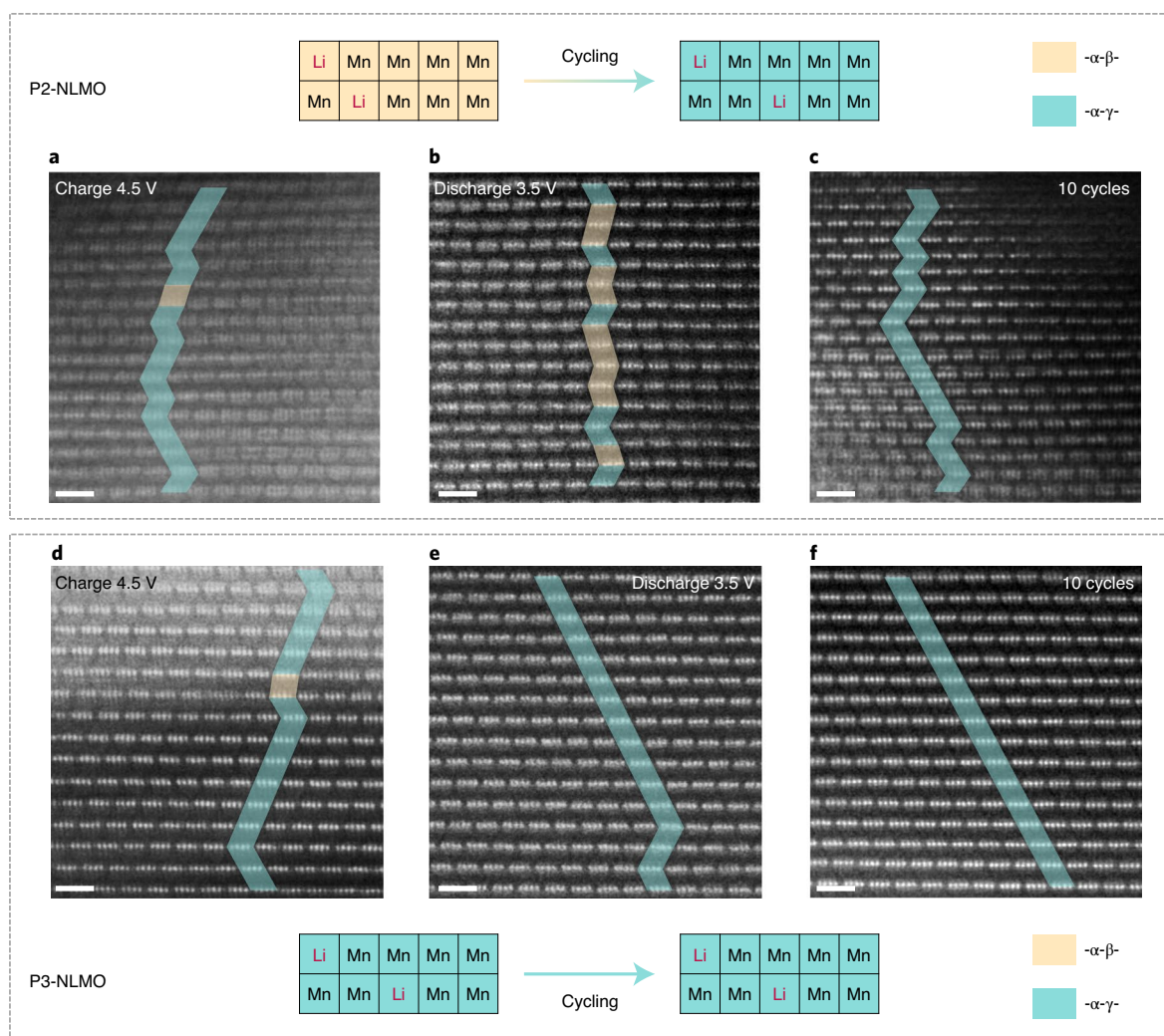


Fig. 3 | Evolution of the ODT structures in P2- and P3- $\text{NaLi}_{0.2}\text{Mn}_{0.8}\text{O}_2$ cathodes on cycling. a–c, P2-type. The stacking model of TM layers transformed from $-\alpha-\beta-$ to $-\alpha-\gamma-$ sequences on Na-ion deintercalation. HAADF-STEM images of the P2-NLMO at first-charged (4.5 V) (a), first-discharged (3.5 V) (b) and tenth-discharged (3.5 V) (c) states. **d–f,** P3-type. The stacking model of TM layers maintained $-\alpha-\gamma-$ sequences on Na-ion deintercalation. HAADF-STEM images of P3-NLMO at first-charged (4.5 V) (d), first-discharged (3.5 V) (e) and tenth-discharged (3.5 V) (f) states. These samples were collected ex situ at different states indicated in Fig. 1e,f by red circles. Scale bars, 1 nm.

on charging and discharging in P2-NLMO. According to the results of the DFT calculations and the experiments, the pristine structure of P2-NLMO was characterized by $-\alpha-\beta-$ stacks, with four Na2 sites and two Na3 sites existing in the Na layer, on the basis of our constructed unit cell (Figs. 4a and 2d,e and Supplementary Fig. 7f(i)). Meanwhile, according to the electrochemistry results, during the charging process, approximately 0.4 Na ions were removed from P2-NLMO (Fig. 1e), where the phase transition from P2 to O2 was verified through desodiation³⁴. The automatic conversion from a P2- $\text{Na}_{12}\text{Li}_4\text{Mn}_{16}\text{O}_{40}$ to a O2- $\text{Na}_{12}\text{Li}_4\text{Mn}_{16}\text{O}_{40}$ model was also reproduced in the relaxation process using DFT calculations (Supplementary Fig. 24). The phase transition from P2 to O2 was further verified by ex situ X-ray diffraction and STEM (Supplementary Figs. 15–18 and Supplementary Note 2).

Figure 4e shows six possible glide paths from P2 to O2 in the TM layer, which form $-\alpha-\alpha-$, $-\alpha-\beta-$ or $-\alpha-\gamma-$ stacks in the O2 structure. As the Li^+ ions in the TM layer migrate into the Na layer in charged states^{31,34}, the $-\alpha-\alpha-$ and $-\alpha-\beta-$ stacks will tend to be prohibited because of the Coulomb repulsion between Li^+ and Na^+ ions (Supplementary Fig. 24). Meanwhile, the paths can be classified as edge-shared (e) or face-shared (f) between the NaO_6 and the TMO_6

octahedra in the O2 structure⁵⁰. Here, the remaining Na^+ ions preferred to occupy Na1 sites rather than Na2 sites in the O2 structure (Supplementary Fig. 25), leading to the prohibitive face-shared paths (Fig. 4e). Thus, only one glide path was feasible (represented by the green arrow in Fig. 4e), and the resulting O2 structure presented $-\alpha-\gamma-$ stacks and edge-sharing between NaO_6 and under the TMO_6 octahedron (Fig. 4b), which explains the $-\alpha-\gamma-$ stacks observed in the charged states (4.5 V versus Na^+/Na), as shown in Fig. 3a. When the Na^+ ions were reinserted into O2- $\text{Na}_{0.2}\text{Li}_{0.2}\text{Mn}_{0.8}\text{O}_2$, there were three paths to return to the P2 structure (Fig. 4f), which formed $-\alpha-\beta-$, $-\alpha-\gamma-$ or $-\alpha(-\gamma)-$ stacks in the P2 structure, as shown in Fig. 4c,d. As noted above, partial Na2 sites were inhibited by the Coulomb repulsion between the Na^+ ions in the $-\alpha-\gamma-$ model (Fig. 4d and Supplementary Fig. 7e), which led to a higher energy of +204 meV per cell, implying a labile structure. Thus, compared with the $-\alpha-\beta-$ model (Fig. 4c and Supplementary Fig. 7f(i)), the $-\alpha-\gamma-$ model with a higher energy corresponds to the lower redox potential. Within the voltage range of ~3.5–4.5 V, the $-\alpha-\gamma-$ model accommodated less than 0.4 Na^+ ions (Fig. 4d), even though both stacking models presented a P2-type structure (for details see ‘Oxygen redox analysis’ in Methods). This implies that the ODT structure of pristine

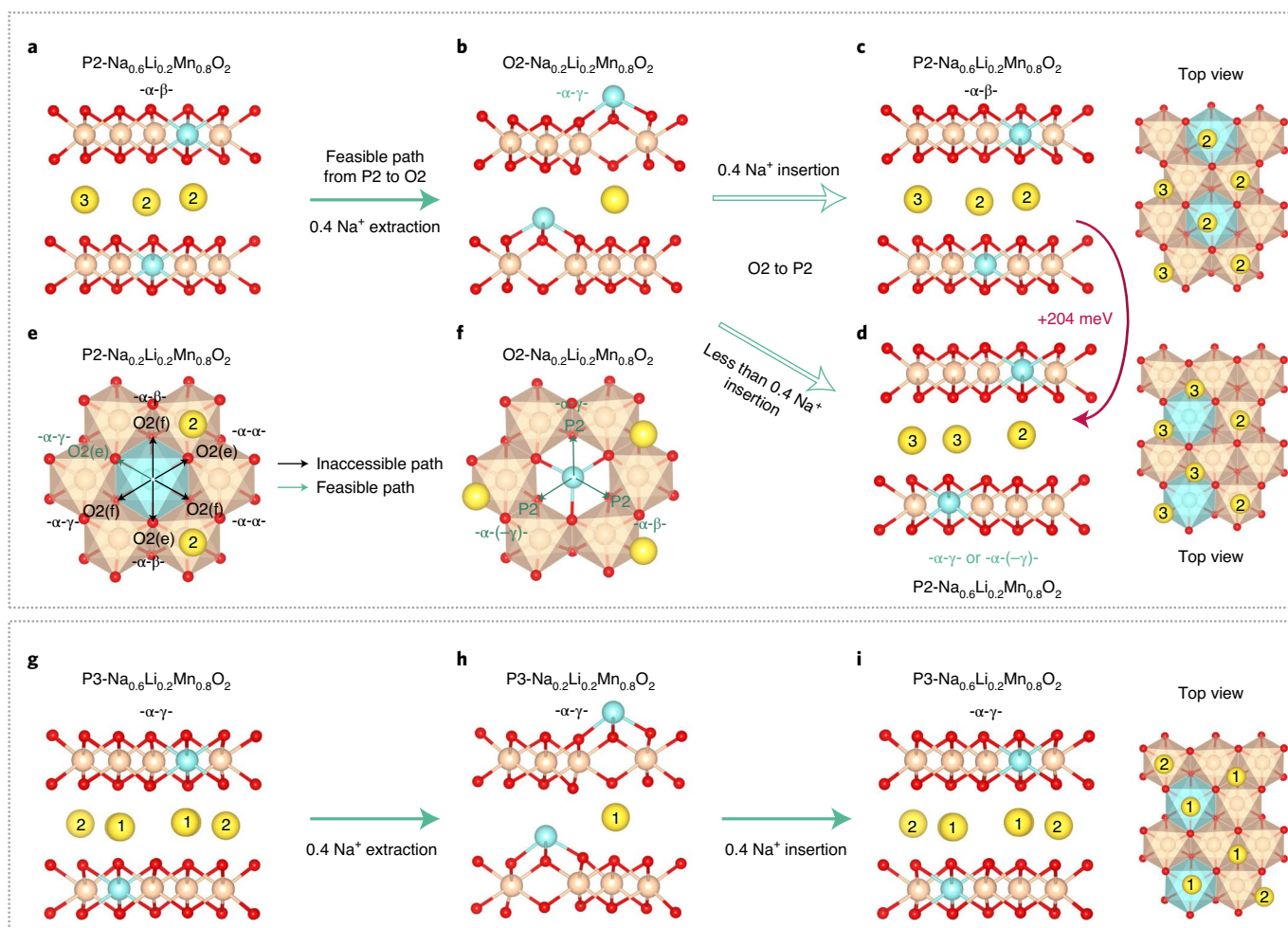


Fig. 4 | Topological protection mechanism during Na-ion deintercalation. a–f, P2-type. **a,** Pristine P2-NLMO structure with the $-\alpha-\beta-$ sequence. **b,** $\text{O2-Na}_{0.2}\text{Li}_{0.2}\text{Mn}_{0.8}\text{O}_2$ structure with the $-\alpha-\gamma-$ sequence at the state of charge of 4.5 V. **c,** P2-NLMO structure with the $-\alpha-\beta-$ sequence at the state of discharge of 3.5 V (the top view is shown in the right panel). **d,** P2-NLMO structure with the $-\alpha-\gamma-$ sequence at the state of discharge of 3.5 V (the top view is shown in the right panel). **e,** Glide paths from the P2 structure to O2 structure (a→b). O2(e) or O2(f) refers to the Na ion occupying an edge/face-shared octahedron in the O2 structure, where the face is coplanar with LiO_6 or MnO_6 . **f,** Glide paths from the O2 structure to P2 structure (b→c or d). **g–i,** P3-type. **g,** Pristine P3-NLMO structure with the $-\alpha-\gamma-$ sequence. **h,** $\text{P3-Na}_{0.2}\text{Li}_{0.2}\text{Mn}_{0.8}\text{O}_2$ structure with the $-\alpha-\gamma-$ sequence at the state of charge of 4.5 V. **i,** P3-NLMO structure with the $-\alpha-\gamma-$ sequence at the state of discharge of 3.5 V (the top view is shown in the right panel). The cyan ball is the Li ion, the brown ball the Mn ion, the yellow ball the Na ion and the red ball the O ion. The number of Na ions represents the type of Na ions, as shown in Supplementary Fig. 9.

P2-NLMO evolved gradually from $-\alpha-\beta-$ stacks to $-\alpha-\gamma-$ stacks on cycling (Fig. 3b,c), which revealed the origin of the rapid capacity decay during cycling in the case of P2-NLMO (Fig. 1e).

Meanwhile, the P3-NLMO structure underwent entirely different stack evolution during Na-ion deintercalation. Figure 4g–i presents the evolution of ODT structures on charging and discharging in P3-NLMO. The pristine structure of P3-NLMO was characterized by $-\alpha-\gamma-$ stacks, which was in agreement with the DFT calculations and the experimental results, in which four Na1 sites and two Na2 sites existed in the Na layer, on the basis of our constructed unit cell (Figs. 4g and 2g,h and Supplementary Fig. 8f(iii)). Our previous study¹⁹ demonstrated that the character of the P3-layered structure could be maintained after the initial charge for P3-NLMO, indicating that the framework of Na-containing layered oxides was stable for LOR. The stable P3 phase was further verified by ex situ X-ray diffraction and STEM (Supplementary Figs. 19–23 and Supplementary Note 2). According to the electrochemistry results, during the charging process, approximately 0.4 Na^+ ions were removed from P3-NLMO (Fig. 1f). Figure 4h shows the optimized

desodiated phase of $\text{P3-Na}_{0.2}\text{Li}_{0.2}\text{Mn}_{0.8}\text{O}_2$ with successive migration of Li^+ ions into the Na layer, which retained the $-\alpha-\gamma-$ stacks. When Na-ion reinsertion occurs, the structure can return to a pristine structure with $-\alpha-\gamma-$ stacks, which guarantees the reversible Na^+ -ion storage. The above evolution process agrees with the STEM results in that the TM layer stacks in P3-NLMO always maintained $-\alpha-\gamma-$ sequences on cycling (Fig. 3d–f), that is, the ODT structure was maintained during the entire cycling process. On comparing the evolution of the ODT structures in P2- and P3-NLMO, the topological features of the $-\alpha-\gamma-$ stacks were found to provide topological protection for reversible LOR on Na-ion deintercalation in P3-NLMO, whereas the $-\alpha-\beta-$ stacks in P2-NLMO did not.

Discussion

Manganese is a promising element due to its resource-abundant, non-toxic, low-cost, and compatible characteristics with LOR, which could satisfy the requirements of the sustainable development of large-scale energy storage. Substituting proper TM elements^{51,52} and designing stable crystal structures³⁴ have been

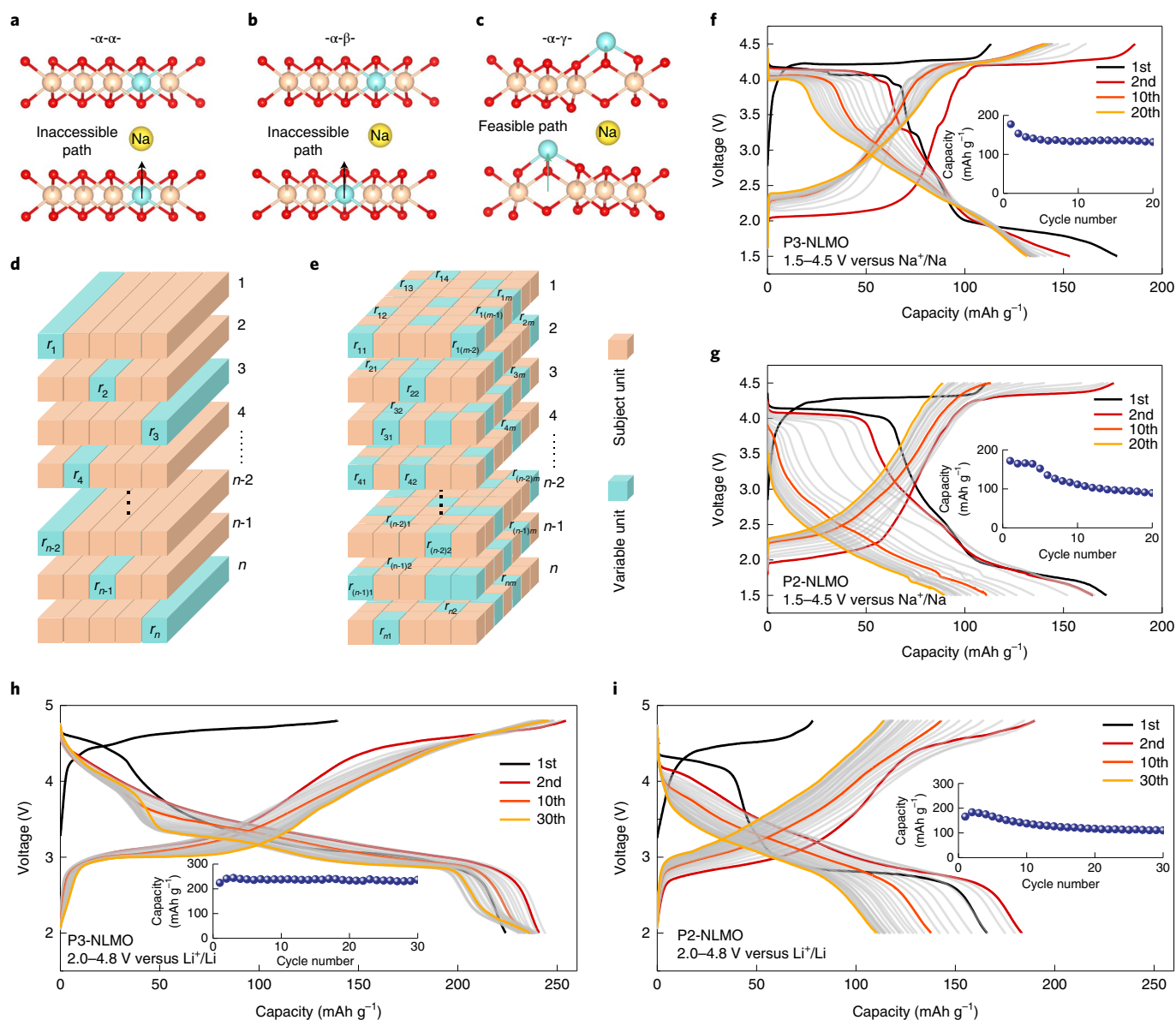


Fig. 5 | Topological order. **a–c**, The structures at the charged states with $-\alpha-\alpha-$ (**a**), $-\alpha-\beta-$ (**b**) and $-\alpha-\gamma-$ (**c**) sequences. **d**, One-dimensional topological order. **e**, Three-dimensional topological order. **f, g**, Capacity–voltage curves of 20 cycles for P3- (**f**) and P2-NLMO (**g**) in the voltage range of 1.5–4.5 V at 10 mA g^{-1} in a Na half-cell. **h, i**, Capacity–voltage curves of 30 cycles for P3- (**h**) and P2-NLMO (**i**) in the voltage range of 2.0–4.8 V at 10 mA g^{-1} in a Li half-cell. Inset shows the capacity retention over cycles.

considered as effective strategies to enhance LOR reversibility, but still could not meet the practical demands at present, while a thorough understanding of LOR is also lacking. Here, we have demonstrated that the topological protection mechanism controls the reversible Na storage with LOR by comparing P2- and P3-NLMO. The ordered arrangement of Li/Mn in the TM layer constituted the ribbon-ordered structure in the intralayer (Fig. 1a). As a result of the incorporation of Li^+ ions into the TM layers, the stacks between the layers generated ODT structures, including $-\alpha-\alpha-$, $-\alpha-\beta-$ and $-\alpha-\gamma-$ sequences (Fig. 2a). In high-charged states, the LOR process is coupled with Li^+ -ion migration from the TM layers to the Na layers^{31,34}, which is feasible in $-\alpha-\gamma-$ stacks (Fig. 5c), but is suppressed in $-\alpha-\alpha-$ or $-\alpha-\beta-$ stacks (Fig. 5a,b) because of the Coulomb repulsion between the alkali metal ions. Further, the accessibility of Li^+ -ion migration in different ODT structures was also validated by Li migration barriers via the CINEB method (Supplementary Fig. 26). In short, the topological feature of $-\alpha-\gamma-$ stacks provides topological

protection for reversible LOR, whereas that of other stacks does not. The structure with $-\alpha-\alpha-$ or $-\alpha-\beta-$ stacks will be transformed into $-\alpha-\gamma-$ stacks on charging, as is the case with, for example, P2-NLMO (a→b in Fig. 4). In the discharging process, the structure cannot be fully restored to $-\alpha-\beta-$ stacks (b→d in Fig. 4), and the ODT structure of pristine P2-NLMO will change. However, the $-\alpha-\gamma-$ model accommodates less Na^+ ions than the $-\alpha-\beta-$ model in the case of P2-NLMO, thus accelerating the capacity decay during cycling. In contrast, the structure always maintains $-\alpha-\gamma-$ stacks in P3-NLMO, thus guaranteeing cycle stability. In general, the protected topological state is revealed in P3-NLMO through the evolution of P2- and P3-type structures.

Furthermore, the ODT structure can be present in different phases. For example, in our study, both $-\alpha-\beta-$ and $-\alpha-\gamma-$ models could exist in P2-NLMO, whereas an $-\alpha-\gamma-$ model also exists in P2-, O2- and P3-NLMO. In fact, this ODT structure can be present in any layered material, including O3, O1, P3, O2, O2' and P2. We

defined a new order parameter of layered cathodes, namely, topological order (R), to describe the interaction between heterogeneous TM layers, independent of the conventional phase definition (O- or P-type). Taking the ODT structure of the P3-NLMO as an example, the position of the Li^+ -ion string within the layer is denoted by r_n , where n is the serial number of the layers (Fig. 5d). Then, the topological order (R^T , transposed matrix) of P3-NLMO can be described as the following matrix:

$$R^T = [r_1 \ r_2 \ r_3 \ r_4 \ \cdots \ r_{n-2} \ r_{n-1} \ r_n] \quad (1)$$

For the P3-NLMO structure with an $-\alpha-\gamma-$ stack, R_{P3}^T is equal to $[1 \ 3 \ 5 \ \cdots \ 2q + 1]$, where q is the integer. The ODT structure of P3-NLMO with the topological order R_{P3}^T is protected on cycling, thus guaranteeing cycle stability. In contrast, the ODT structure of P2-NLMO with $R_{P2}^T = [1 \ 2 \ 3 \ \cdots \ q]$ is broken, thus diminishing the performance. To further verify the role of topological order R_{P3}^T in enhancing the reversibility of LOR, the electrochemical properties of P3- and P2-NLMO were examined versus metallic Na or Li in a Na or Li half-cell. The P3-NLMO cathode in the Na half-cell delivered a high discharge capacity of $\sim 177 \text{ mAh g}^{-1}$ within the voltage range of 1.5–4.5 V at 10 mA g^{-1} , as shown in Fig. 5f, exhibiting 74% capacity retention after 20 cycles. As a comparison, the P2-NLMO cathode in the Na half-cell showed a discharge capacity of 171 mAh g^{-1} with 52% capacity retention after 20 cycles (Fig. 5g). Surprisingly, the P3-NLMO cathode in the Li half-cell delivered a reversible capacity of $\sim 240 \text{ mAh g}^{-1}$ at the second cycle within the voltage range of 2.0–4.8 V at 10 mA g^{-1} , exhibiting 98% capacity retention after 30 cycles, as shown in Fig. 5h. In contrast, a capacity of $\sim 183 \text{ mAh g}^{-1}$ was obtained in P2-NLMO with only 60% capacity retention after 30 cycles, as shown in Fig. 5i. The excellent cycling performance in Na and Li half-cells once again proves the importance of topological protection for LOR.

This concept of topological order could be extended to the three-dimensional case, as shown in Fig. 5e (for details see ‘Three-dimensional topological order’ in Methods). As popular layered materials, ternary cathodes benefit from the synergistic effect of Ni, Co and Mn (Al) elements, which results in superior performance^{53,54}, and numerous elements tend to be used as dopants to improve the performance of the electrodes^{29,55,56}. For these materials with LOR, the incorporation of Li, Na, Mg, vacancy, etc. into the TM layer^{8,57} triggers and/or stabilizes the LOR process. In different systems, it is of great scientific significance to design and control the variable units or topological order (R) to improve the performance of the materials. There are different factors affecting the topological order (R), related to not only the type and content of the elements involved, but also the synthesis conditions. For example, although having the same composition and Li/Mn ordering within the layers of both P2- and P3-NLMO materials, the synthesis temperature affects the stacking sequences (topological order (R)). In addition, the coordination environment of the Li^+ and Na^+ ions and their migration, as well as the main structural network (honeycomb, ribbon, etc.), all have an impact on the topological structures. The design concept of topology is based on long-range interactions between heterogeneous units and distinguishes itself from traditional methods of performance improvement (doping, coating, interfacial design, etc.). It is undeniable that the topology needs to be designed in terms of the overall structure. In general, as a new degree of freedom, the topological order (R) will have an effective, almost ‘magical’ impact on preserving the cycle reversibility for layered materials, and even more so for electrode materials, thus presenting a compelling strategy in the search for high energy-density cathode materials.

In summary, we have revealed the key role of topological protection in enhancing the reversibility of LOR by investigating P2- and P3- $\text{Na}_{0.6}\text{Li}_{0.2}\text{Mn}_{0.8}\text{O}_2$. The topological feature of $-\alpha-\gamma-$ stacks provides

topological protection for reversible LOR on Na-ion deintercalation in P3-NLMO, whereas the topological feature of $-\alpha-\beta-$ stacks in pristine P2-NLMO is broken and evolves gradually from $-\alpha-\beta-$ stacks to $-\alpha-\gamma-$ stacks on cycling, which accommodate fewer Na ions and leads to capacity decay. In particular, the P3-NLMO cathode delivers a high capacity of 240 mAh g^{-1} with outstanding cycling stability in a lithium half-cell. The protected topological state is identified in terms of the topological order $R^T = [1 \ 3 \ 5 \ \cdots \ 2q + 1]$, a new order parameter of layered cathodes describing the interaction between heterogeneous TM layers, which differs from the conventional phase definition (O- or P-type). This work provides guidance on the identification of reversible Mn-rich cathode materials for sustainable batteries. In a broader context, our findings define a direction for materials design in applications beyond rechargeable batteries, such as electrocatalysts⁵⁸, photovoltaics⁵⁹ and fuel cells⁶⁰, where the topological order (R) could play a critical role.

Methods

Material synthesis. The solid-state reaction method was used to obtain the P3-type and P2-type $\text{Na}_{0.6}[\text{Li}_{0.2}\text{Mn}_{0.8}]\text{O}_2$ powder samples. Na_2CO_3 (99.9%, Alfa, 2% excess), LiOH (98%, Alfa, 2% excess) and MnO_2 (99.9%, Alfa) were ground to homogeneous mixtures, which were then calcined in an air atmosphere. The holding temperature was set to be 700°C for P3-type $\text{Na}_{0.6}[\text{Li}_{0.2}\text{Mn}_{0.8}]\text{O}_2$ and 900°C for P2-type $\text{Na}_{0.6}[\text{Li}_{0.2}\text{Mn}_{0.8}]\text{O}_2$, with a heating (12 h) and cooling rate of 2°C min^{-1} .

Electrochemical measurements. The electrodes were fabricated via roller pressing the mixture of active material (80 wt%), carbon nanotube (15 wt%) and polytetrafluoroethylene (5 wt%), which was then cut into isometric square pieces. CR2032 coin cells were assembled in an Ar-filled glovebox to evaluate the charge and discharge behaviours on a Land CT2001A battery test system, with Na or Li metal foil as the counter electrode and glass fibre as the separator. 1 M NaClO_4 in ethylene:dimethyl carbonate:propylene carbonate (1:1:1 in volume) with fluoroethylene carbonate (2 vol%) and 1 M LiPF_6 in ethylene:dimethyl carbonate (1:1 in volume) were used as the electrolyte for Na half-cells and Li half-cells, respectively.

Materials characterization. The neutron data were measured at the Multiple Physics Instrument at the China Spallation Neutron Source. Roughly 2 g of sample was measured for 6 h at ambient conditions. GSAS2 was used to refine the neutron data. The structure was characterized using a D8 Bruker X-ray diffractometer with CuK_α radiation ($\lambda = 1.5405 \text{ \AA}$) in the scan range (2θ) of 10° – 80° . The Na, Li and Mn ratio of samples was measured using an ICP-MS 7700 (Agilent Technologies). An ARM-200F (JEOL) transmission electron microscope (operated at 200 keV and equipped with double spherical aberration (Cs) correctors) was used for the spherical aberration-corrected STEM test, with both HAADF and ABF techniques. The attainable resolution of the probe defined by the objective prefield was 78 picometres, and the ABF and HAADF images were acquired at acceptance angles of 11 – 22 and 90 – 370 mrad , respectively. All the ABF and HAADF images in this paper were Fourier-filtered to minimize the effect of the contrast noise, which did not have any effect on our measurement results. Ex situ hard X-ray absorption spectroscopy (hXAS) and ex situ soft XAS experiments were performed at beamline BL14W and BL02B02 at the Shanghai Synchrotron Radiation Facility. The ex situ hXAS tests were carried out in transmission mode with a Si(111) double-crystal monochromator, which was detuned to the 35% value of its original maximum intensity to eliminate the higher order harmonics. ATHENA software package was employed to analyse the X-ray absorption near edge structure (XANES) results. Raman spectra were collected by using a JY-HR 800 (Jobin Yvon) equipped with a diode laser ($\lambda = 532 \text{ nm}$) at room temperature.

Calculation details. The Vienna Ab initio Simulation Package^{61–63} based on DFT was used for the first-principles calculations. Electronic exchange–correlation interaction, along with the GGA functional in the parameterization of the Perdew–Burke–Ernzerhof pseudopotential⁶⁴, was dealt with projector augmented wave⁶⁵ potentials. A plane wave representation for the wave function with a cut-off energy of 500 eV was applied. Geometry optimizations were performed using a conjugate gradient minimization until all the forces acting on the ions were less than 0.01 eV \AA^{-1} per atom. The K-point mesh with a spacing of $\sim 0.03 \text{ \AA}^{-1}$ was adopted. The Li migration barrier energy was calculated by the CINEB method with five images as intermediate states. The crystal structures were built using VESTA software⁶⁶. The crystal orbital Hamilton population was computed with DFT calculations by the Lobster program⁶⁷.

Oxygen redox analysis. The charge compensation of the two cathodes in the voltage range 3.5–4.5 V is mainly attributed to the reversible LOR, which has been adequately demonstrated by many advanced characterizations (hard and soft X-ray

absorption spectroscopy, resonant inelastic X-ray scattering, scanning transmission X-ray microscopy, etc.)^{19,34,42}, making it possible to assess the reversibility of LOR with the voltage plateau capacity as the measure. Different from the materials with long-slope discharge voltage profiles, such as P2-Na_{2/3}[Mg_{0.28}Mn_{0.72}]O₂ (ref. 11) and P2-Na_{0.72}[Li_{0.28}Mn_{0.72}]O₂ (ref. 68) working in a wide voltage range (1.5–4.5 V or 2.0–4.5 V) with mixed oxygen and manganese electrochemistry, P2-NLMO and P3-NLMO with separated redox voltage are almost the perfect objects of study to investigate the LOR mechanism on its own.

The charge compensation mechanism in P2- and P3-NLMO was further revealed by DFT calculations. As shown in Supplementary Fig. 27a, the interlayer O–O distance was approximately 2.55 Å for the oxygen ions coordinated with two Mn⁴⁺ ions and one Li⁺ ion in pristine P2-NLMO. An increased partial density of states can be found close to the Fermi level for O ions because of the specific Na–O–Li configuration¹². Here, when charged to 4.5 V, the P2 structure was transformed into an O2 structure with a decrease in the O–O distance (2.48 Å). Meanwhile, electron holes emerged at the O 2p orbital, implying oxidized O²⁻ ions. On discharging, partial holes at the O 2p orbital were retained because of the irreversibility of Na⁺ ions, whereas the O–O distance increased slightly to 2.49 Å. A more detailed evolution of the electronic structures of P2-NLMO is shown in Supplementary Figs. 28 and 29 and Supplementary Note 3. Similarly, the interlayer O–O distance decreased from 2.54 to 2.48 Å in P3-NLMO during charging, as shown in Supplementary Fig. 27b. As a result of the good reversibility, the O–O distance recovered to a pristine 2.54 Å. The charge compensation mechanism of the O–O pairs in P3-NLMO was consistent with our previous experimental results¹⁹. Meanwhile, the valence state of Mn in P3-NLMO was shown to remain unchanged on charge/discharge via various spectroscopic techniques¹⁹. Supplementary Fig. 30 shows the Mn K-edge XANES results of P2-NLMO samples in different states of charge/discharge. There is no obvious absorption edge shift during charge and discharge, which indicates that the valence states of Mn remain unchanged. The same conclusion could also be demonstrated by Mn L-edge X-ray absorption spectroscopy, as shown in Supplementary Fig. 31, showing consistent L3 and L2 edge positions. These results indicate that in the voltage range 3.5–4.5 V (versus Na⁺/Na) the charge compensation is not related to Mn redox.

The specific capacity from LOR in P3-NLMO also declined gradually with the electrochemical cycle, which has been verified in previous reports^{7,19,42}. The STEM images suggested that no clear TM migration or cracking occurred in the P2- and P3-NLMO samples after ten cycles (Supplementary Fig. 32). The Raman spectrum of the Mn–O bond in P3-NLMO (Supplementary Fig. 33) broadened and weakened at the state of charge (4.5 V) resulting from the lattice distortion induced by LOR. And the peak became sharp again when discharged to 3.5 V (Supplementary Fig. 33), corresponding to the reversible structure evolution. In fact, Yang and coworkers⁴² proposed that the substantial capacity loss stems from non-lattice oxygen oxidation and that the voltage decay can be attributed to an increasing Mn redox contribution on cycling in P3-NLMO.

ODT structures. To predict the stacking models, P2- and P3-type ribbon-ordered structures were first constructed, as shown in Supplementary Figs. 5 and 6, with only the adjacent stacks considered to simplify the calculations. For example, the P2-NLMO model with α - β -stacks contained α - β - and α -(β)-sequences (Supplementary Fig. 7b), forming a Z-type array rather than a linear array of the Li⁺-ion string along the out-of-plane direction. Other P2- and P3-NLMO models are shown in Supplementary Figs. 7a–c and 8a–c. The stacking behaviour directly determines the coordination environment of the Na⁺ ions (for example, octahedron in O-type structures and trigonal prismatic in P-type structures⁶⁹); in turn, the Na⁺-ion configurations also influence the stacking of the TMO₂ layers. In conventional P2 structures (Supplementary Fig. 9), two types of Na sites can be identified: an edge-shared trigonal prismatic cavity (V–Na–V, 3) and a face-shared trigonal prismatic cavity (Mn–Na–Mn, 4)². As a result of the incorporation of Li⁺ ions into the TM layers, the trigonal prism can be coplanar with LiO₆ in addition to MnO₆. The two new Na sites are face-shared trigonal prismatic cavities with LiO₆ (Li–Na–Li, 1) and LiO₆/MnO₆ (Li–Na–Mn, 2). In conventional P3 structures (Supplementary Fig. 9), only one Na site exists, that is, an edge/face-shared trigonal prismatic cavity (Mn–Na–V, 2)⁷⁰. Similarly, Mn can be replaced by Li to generate a new edge/face-shared trigonal prismatic cavity (Li–Na–V, 1), where the face here is coplanar with LiO₆. Before considering the Na-ion configurations in the Na layer, it should be noted that all Na⁺ ions present the most uniform distribution to reduce the Coulomb repulsion^{71,72}. On this basis, the priority of the Na-ion position is assumed to be Na1 > Na2 > Na3 > Na4 in P2-NLMO and Na1 > Na2 in P3-NLMO, as shown in Supplementary Fig. 9. Based on the above principles, a series of structures with different Na-ion distributions were designed to verify these assumptions and to determine the stacking structures in P2- and P3-NLMO, as shown in Supplementary Figs. 7d–f and 8d–f. The energy of the most stable P2-NLMO structure was 0.19 meV atom⁻¹ (Supplementary Fig. 10), with the structure characterized by four Na2 sites and two Na3 sites in the α - β -stacks (Supplementary Fig. 7f(i)). The energy increased to 0.88 meV atom⁻¹ for the structure with two Na2 sites and four Na3 sites in the α - β -stacks, suggesting that Na⁺ ions prefer to occupy Na2 sites rather than Na3 sites (Supplementary Fig. 7f(ii)). This result was further verified by the structure with three Na2 sites and three Na3 sites in the α - β -stack, the energy value of which (0.40 meV atom⁻¹)

was between those of the previous two structures (Supplementary Fig. 7f(iii)). Compared with the α - β - (i) model (Supplementary Fig. 7f(i)), the α - γ - model was more labile with a higher energy of 3.17 meV atom⁻¹, which was attributed to the prohibitive Na2 sites limited by the α - γ -stacks and the Coulomb repulsion. In terms of the P3-NLMO structure, the most stable Na⁺ ion distribution (0.00 meV atom⁻¹) was characterized by four Na1 sites and two Na2 sites in the α - γ -stacks (Supplementary Figs. 10 and 8f(iii)). In such a model, the Na2 sites can be set to two alternative distributions, as shown in Supplementary Fig. 8f(i,ii), which both present an energy of 0.50 meV atom⁻¹, thus implying a precisely equivalent position. However, the energy increase from 0.00 to 0.50 meV atom⁻¹ suggested that a cross-distribution (Supplementary Fig. 8f(iii)) was preferred. Like the P2-NLMO structure, partial Na1 sites were inhibited by the Coulomb repulsion between the Na⁺ ions in the α - β -stacks (Supplementary Fig. 8e). Thus, the structure with α - β -stacks had two Na1 sites and four Na2 sites with a higher energy of 4.25 meV atom⁻¹. On the basis of DFT calculations, the most stable ODT structures of pristine P2- and P3-NLMO were predicted to be α - β - and α - γ -stacks, respectively, but only adjacent stacks were considered. To ensure alignment with the linear model of the Li⁺-ion string along the interplane (Fig. 2b), the optimized structure of P2- and P3-NLMO were transformed from Z-type models into linear-type models (Supplementary Fig. 11), with the side and top views of the optimized P2- and P3-NLMO structures shown in Fig. 2c,f.

Three-dimensional topological order. The variable unit in the heterogeneous layer is located at r_{nm} , where n and m are the serial number of layers and variable units, respectively (Fig. 5e). The three-dimensional topological order (R) can be described as the following matrix:

$$R = \begin{pmatrix} r_{11} & r_{12} & r_{13} & r_{14} & \cdots & r_{1(m-2)} & r_{1(m-1)} & r_{1m} \\ r_{21} & r_{22} & r_{23} & r_{24} & \cdots & r_{2(m-2)} & r_{2(m-1)} & r_{2m} \\ r_{31} & r_{32} & r_{33} & r_{34} & \cdots & r_{3(m-2)} & r_{3(m-1)} & r_{3m} \\ r_{41} & r_{42} & r_{43} & r_{44} & \cdots & r_{4(m-2)} & r_{4(m-1)} & r_{4m} \\ \vdots & \vdots & \vdots & \vdots & \ddots & \vdots & \vdots & \vdots \\ r_{(n-2)1} & r_{(n-2)2} & r_{(n-2)3} & r_{(n-2)4} & \cdots & r_{(n-2)(m-2)} & r_{(n-2)(m-1)} & r_{(n-2)m} \\ r_{(n-1)1} & r_{(n-1)2} & r_{(n-1)3} & r_{(n-1)4} & \cdots & r_{(n-1)(m-2)} & r_{(n-1)(m-1)} & r_{(n-1)m} \\ r_{n1} & r_{n2} & r_{n3} & r_{n4} & \cdots & r_{n(m-2)} & r_{n(m-1)} & r_{nm} \end{pmatrix} \quad (2)$$

Here, the variable units within the layer can be doped element, vacancy, lattice distortion, charge, electron spin states and so on.

Data availability

The data that support the findings detailed in this study are available in the article and its Supplementary Information or from the corresponding authors on reasonable request.

Received: 18 April 2021; Accepted: 13 October 2021;

Published online: 02 December 2021

References

- Lee, J. et al. Reversible Mn²⁺/Mn⁴⁺ double redox in lithium-excess cathode materials. *Nature* **556**, 185–190 (2018).
- Zhao, C. et al. Rational design of layered oxide materials for sodium-ion batteries. *Science* **370**, 708–711 (2020).
- Zhu, X. et al. LiMnO₂ cathode stabilized by interfacial orbital ordering for sustainable lithium-ion batteries. *Nat. Sustain.* **4**, 392–401 (2021).
- Hu, E. et al. Evolution of redox couples in Li- and Mn-rich cathode materials and mitigation of voltage fade by reducing oxygen release. *Nat. Energy* **3**, 690–698 (2018).
- Hua, W. et al. Structural insights into the formation and voltage degradation of lithium- and manganese-rich layered oxides. *Nat. Commun.* **10**, 5365 (2019).
- Yabuuchi, N. et al. High-capacity electrode materials for rechargeable lithium batteries: Li₂NbO₄-based system with cation-disordered rocksalt structure. *Proc. Natl Acad. Sci. USA* **112**, 7650–7655 (2015).
- Du, K. et al. Exploring reversible oxidation of oxygen in a manganese oxide. *Energy Environ. Sci.* **9**, 2575–2577 (2016).
- Assat, G. & Tarascon, J.-M. Fundamental understanding and practical challenges of anionic redox activity in Li-ion batteries. *Nat. Energy* **3**, 373–386 (2018).
- Sathiyaraj, M. et al. Origin of voltage decay in high-capacity layered oxide electrodes. *Nat. Mater.* **14**, 230–238 (2015).
- Li, Q. et al. Dynamic imaging of crystalline defects in lithium-manganese oxide electrodes during electrochemical activation to high voltage. *Nat. Commun.* **10**, 1692 (2019).

11. Maitra, U. et al. Oxygen redox chemistry without excess alkali-metal ions in $\text{Na}_{2/3}[\text{Mg}_{0.28}\text{Mn}_{0.72}]\text{O}_2$. *Nat. Chem.* **10**, 288–295 (2018).
12. Seo, D. H. et al. The structural and chemical origin of the oxygen redox activity in layered and cation-disordered Li-excess cathode materials. *Nat. Chem.* **8**, 692–697 (2016).
13. Hong, J. et al. Metal–oxygen decoordination stabilizes anion redox in Li-rich oxides. *Nat. Mater.* **18**, 256–265 (2019).
14. Sathiya, M. et al. Reversible anionic redox chemistry in high-capacity layered-oxide electrodes. *Nat. Mater.* **12**, 827–835 (2013).
15. Saubanère, M., McCalla, E., Tarascon, J. M. & Doublet, M. L. The intriguing question of anionic redox in high-energy density cathodes for Li-ion batteries. *Energy Environ. Sci.* **9**, 984–991 (2016).
16. Xie, Y., Saubanère, M. & Doublet, M. L. Requirements for reversible extra-capacity in Li-rich layered oxides for Li-ion batteries. *Energy Environ. Sci.* **10**, 266–274 (2017).
17. Vergnet, J., Saubanère, M., Doublet, M.-L. & Tarascon, J.-M. The structural stability of P2-layered Na-based electrodes during anionic redox. *Joule* **4**, 420–434 (2020).
18. McCalla, E. et al. Visualization of O–O peroxo-like dimers in high-capacity layered oxides for Li-ion batteries. *Science* **350**, 1516–1521 (2015).
19. Rong, X. et al. Structure-induced reversible anionic redox activity in Na layered oxide cathode. *Joule* **2**, 125–140 (2018).
20. Yahia, M. B., Vergnet, J., Saubanère, M. & Doublet, M.-L. Unified picture of anionic redox in Li/Na-ion batteries. *Nat. Mater.* **18**, 496–502 (2019).
21. Chen, Z., Li, J. & Zeng, X. C. Unraveling oxygen evolution in Li-rich oxides: a unified modeling of the intermediate peroxo/superoxo-like dimers. *J. Am. Chem. Soc.* **141**, 10751–10759 (2019).
22. Yabuuchi, N. et al. Origin of stabilization and destabilization in solid-state redox reaction of oxide ions for lithium-ion batteries. *Nat. Commun.* **7**, 13814 (2016).
23. Luo, K. et al. Charge-compensation in 3d-transition-metal-oxide intercalation cathodes through the generation of localized electron holes on oxygen. *Nat. Chem.* **8**, 684–691 (2016).
24. Jacquet, Q. et al. Charge transfer band gap as an indicator of hysteresis in Li-disordered rock salt cathodes for Li-ion batteries. *J. Am. Chem. Soc.* **141**, 11452–11464 (2019).
25. Okubo, M. & Yamada, A. Molecular orbital principles of oxygen-redox battery electrodes. *ACS Appl. Mater. Interfaces* **9**, 36463–36472 (2017).
26. Radin, M. D., Vinckeviciute, J., Seshadri, R. & Van der Ven, A. Manganese oxidation as the origin of the anomalous capacity of Mn-containing Li-excess cathode materials. *Nat. Energy* **4**, 639–646 (2019).
27. Eum, D. et al. Voltage decay and redox asymmetry mitigation by reversible cation migration in lithium-rich layered oxide electrodes. *Nat. Mater.* **19**, 419–427 (2020).
28. Lee, J. et al. Unlocking the potential of cation-disordered oxides for rechargeable lithium batteries. *Science* **343**, 519–522 (2014).
29. Lee, J. et al. A new class of high capacity cation-disordered oxides for rechargeable lithium batteries: Li–Ni–Ti–Mo oxides. *Energy Environ. Sci.* **8**, 3255–3265 (2015).
30. Lee, J. et al. Mitigating oxygen loss to improve the cycling performance of high capacity cation-disordered cathode materials. *Nat. Commun.* **8**, 981 (2017).
31. Wang, Q. et al. Unlocking anionic redox activity in O3-type sodium 3d layered oxides via Li substitution. *Nat. Mater.* **20**, 353–361 (2021).
32. Mortemard de Boisse, B. et al. Intermediate honeycomb ordering to trigger oxygen redox chemistry in layered battery electrode. *Nat. Commun.* **7**, 11397 (2016).
33. Mortemard de Boisse, B. et al. Coulombic self-ordering upon charging a large-capacity layered cathode material for rechargeable batteries. *Nat. Commun.* **10**, 2185 (2019).
34. House, R. A. et al. Superstructure control of first-cycle voltage hysteresis in oxygen-redox cathodes. *Nature* **577**, 502–508 (2019).
35. House, R. A. et al. First-cycle voltage hysteresis in Li-rich 3d cathodes associated with molecular O_2 trapped in the bulk. *Nat. Energy* **5**, 777–785 (2020).
36. Blanco-Redondo, A., Bell, B., Oren, D., Eggleton, B. J. & Segev, M. Topological protection of biphoton states. *Science* **362**, 568–571 (2018).
37. Peterson, C. W., Li, T., Jiang, W., Hughes, T. L. & Bahl, G. Trapped fractional charges at bulk defects in topological insulators. *Nature* **589**, 376–380 (2021).
38. Seidel, J. Nanoelectronics based on topological structures. *Nat. Mater.* **18**, 188–190 (2019).
39. Kanyolo, G. M. et al. Honeycomb layered oxides: structure, energy storage, transport, topology and relevant insights. *Chem. Soc. Rev.* **50**, 3990–4030 (2021).
40. Masese, T. et al. Topological defects and unique stacking disorders in honeycomb layered oxide $\text{K}_2\text{Ni}_2\text{TeO}_6$ nanomaterials: implications for rechargeable batteries. *ACS Appl. Nano Mater.* **4**, 279–287 (2021).
41. Huang, J. et al. Non-topotactic reactions enable high rate capability in Li-rich cathode materials. *Nat. Energy* **6**, 706–714 (2021).
42. Wu, J. et al. Dissociate lattice oxygen redox reactions from capacity and voltage drops of battery electrodes. *Sci. Adv.* **6**, eaaw3871 (2020).
43. Han, M. et al. Stacking faults hinder lithium insertion in Li_2RuO_5 . *Adv. Energy Mater.* **10**, 2002631 (2020).
44. Yu, H. et al. Crystalline grain interior configuration affects lithium migration kinetics in Li-rich layered oxide. *Nano Lett.* **16**, 2907–2915 (2016).
45. Zhang, Q. et al. Atomic-resolution imaging of electrically induced oxygen vacancy migration and phase transformation in $\text{SrCoO}_{2.5-\delta}$. *Nat. Commun.* **8**, 104 (2017).
46. Okunishi, E. et al. Visualization of light elements at ultrahigh resolution by STEM annular bright field microscopy. *Microsc. Microanal.* **15**, 164–165 (2009).
47. Zhang, Q. et al. Direct observation of multiferroic vortex domains in YMnO_3 . *Sci. Rep.* **3**, 2741 (2013).
48. Chae, S. C. et al. Evolution of the domain topology in a ferroelectric. *Phys. Rev. Lett.* **110**, 167601 (2013).
49. Choi, T. et al. Insulating interlocked ferroelectric and structural antiphase domain walls in multiferroic YMnO_3 . *Nat. Mater.* **9**, 253–258 (2010).
50. Kubota, K., Kumakura, S., Yoda, Y., Kuroki, K. & Komaba, S. Electrochemistry and solid-state chemistry of NaMeO_2 ($\text{Me} = 3d$ transition metals). *Adv. Energy Mater.* **8**, 1703415 (2018).
51. Xu, J. et al. Elucidating anionic oxygen activity in lithium-rich layered oxides. *Nat. Commun.* **9**, 947 (2018).
52. Nayak, P. K. et al. Al doping for mitigating the capacity fading and voltage decay of layered Li and Mn-rich cathodes for Li-ion batteries. *Adv. Energy Mater.* **6**, 1502398 (2016).
53. Wei, Y. et al. Kinetics tuning of Li-ion diffusion in layered $\text{Li}(\text{Ni}_x\text{Mn}_y\text{Co}_z)\text{O}_2$. *J. Am. Chem. Soc.* **137**, 8364–8367 (2015).
54. Zheng, J. et al. Tuning of thermal stability in layered $\text{Li}(\text{Ni}_x\text{Mn}_y\text{Co}_z)\text{O}_2$. *J. Am. Chem. Soc.* **138**, 13326–13334 (2016).
55. Wang, R. et al. A disordered rock-salt Li-excess cathode material with high capacity and substantial oxygen redox activity: $\text{Li}_{1.25}\text{Nb}_{0.25}\text{Mn}_{0.5}\text{O}_2$. *Electrochem. Commun.* **60**, 70–73 (2015).
56. Ma, X., Kang, K., Ceder, G. & Meng, Y. S. Synthesis and electrochemical properties of layered $\text{LiNi}_{1/3}\text{Sb}_{1/3}\text{O}_2$. *J. Power Sources* **173**, 550–555 (2007).
57. House, R. A. et al. The role of O_2 in O-redox cathodes for Li-ion batteries. *Nat. Energy* **6**, 781–789 (2021).
58. Yang, H. B. et al. Atomically dispersed Ni(I) as the active site for electrochemical CO_2 reduction. *Nat. Energy* **3**, 140–147 (2018).
59. Domanski, K. et al. Migration of cations induces reversible performance losses over day/night cycling in perovskite solar cells. *Energy Environ. Sci.* **10**, 604–613 (2017).
60. Ott, S. et al. Ionomer distribution control in porous carbon-supported catalyst layers for high-power and low Pt-loaded proton exchange membrane fuel cells. *Nat. Mater.* **19**, 77–85 (2020).
61. Kresse, G. & Furthmüller, J. Efficient iterative schemes for ab initio total-energy calculations using a plane-wave basis set. *Phys. Rev. B* **54**, 11169–11186 (1996).
62. Kresse, G. & Furthmüller, J. Efficiency of ab-initio total energy calculations for metals and semiconductors using a plane-wave basis set. *Comp. Mater. Sci.* **6**, 15–50 (1996).
63. Shi, S. et al. Multi-scale computation methods: their applications in lithium-ion battery research and development. *Chin. Phys. B* **25**, 018212 (2016).
64. Perdew, J. P., Burke, K. & Ernzerhof, M. Generalized gradient approximation made simple. *Phys. Rev. Lett.* **78**, 1396–1396 (1997).
65. Blöchl, P. E. Projector augmented-wave method. *Phys. Rev. B* **50**, 17953–17979 (1994).
66. Momma, K. & Izumi, F. VESTA 3 for three-dimensional visualization of crystal, volumetric and morphology data. *J. Appl. Crystallogr.* **44**, 1272–1276 (2011).
67. Deringer, V. L., Tchougreff, A. L. & Dronskowski, R. Crystal orbital Hamilton population (COHP) analysis as projected from plane-wave basis sets. *J. Phys. Chem. A* **115**, 5461–5466 (2011).
68. Rong, X. et al. Anionic redox reaction-induced high-capacity and low-strain cathode with suppressed phase transition. *Joule* **3**, 503–517 (2019).
69. Delmas, C., Fouassier, C. & Hagenmüller, P. Structural classification and properties of the layered oxides. *Physica* **99B**, 81–85 (1980).
70. Bianchini, M. et al. The interplay between thermodynamics and kinetics in the solid-state synthesis of layered oxides. *Nat. Mater.* **19**, 1088–1095 (2020).
71. Lee, D. H., Xu, J. & Meng, Y. S. An advanced cathode for Na-ion batteries with high rate and excellent structural stability. *Phys. Chem. Chem. Phys.* **15**, 3304–3312 (2013).
72. Gao, A. et al. K-birnessite electrode obtained by ion exchange for potassium-ion batteries: Insight into the concerted ionic diffusion and K storage mechanism. *Adv. Energy Mater.* **9**, 1802739 (2019).

Acknowledgements

This work was supported by Beijing Natural Science Foundation (Z190010), National Key R&D Program of China (no. 2019YFA0308500), the Strategic Priority Research Program of Chinese Academy of Sciences (grant no. XDB07030200, XDA21070500),

the National Natural Science Foundation of China (grant nos. 51672307, 51991344, 52025025, 52072400, 52002394, 51725206, 11805034, 21704105 and U1930102), Beijing Natural Science Fund-Haidian Original Innovation Joint Fund (L182056), the Basic Science Centre Program of NSFC (grant no. 51788104) and the Natural Science Foundation of Guangdong Province (2017A030313021).

Author contributions

L.G., Y.-S.H. and X.R. designed and supervised the project. X.R. synthesized, characterized (X-ray diffraction, XAS, Raman) and electrochemically tested the samples and analysed the data with X.Y., H.L., C.D., Y.-S.H., C.N. and L.C. Q.Z., X. Li and F.M. performed the STEM measurements and analysed data with A.G., T.S., Z.T., X.W., D.X. and D.S. W.H.K., H.C. and W.Y. performed neutron diffraction measurements and analysed data. A.G. designed and performed DFT calculations and analysed the data with X. Lu and L.G. A.G., X.R., Q.Z., Y.L., Q.Y., J.D., Y.-S.H. and L.G. wrote the manuscript with the help of the other authors. The manuscript reflects the contributions of all authors.

Competing interests

The authors declare no competing interests.

Additional information

Supplementary information The online version contains supplementary material available at <https://doi.org/10.1038/s41893-021-00809-0>.

Correspondence and requests for materials should be addressed to Xiaohui Rong, Yong-Sheng Hu or Lin Gu.

Peer review information *Nature Sustainability* thanks the anonymous reviewers for their contribution to the peer review of this work.

Reprints and permissions information is available at www.nature.com/reprints.

Publisher's note Springer Nature remains neutral with regard to jurisdictional claims in published maps and institutional affiliations.

© The Author(s), under exclusive licence to Springer Nature Limited 2021